Fabrication and analysis of polymer microstructures through ion microprobe techniques

Elis Moura Stori,[1,2] Claudia Telles de Souza,[1] Johnny Ferraz Dias[1]

[1]Ion Implantation Laboratory, Institute of Physics, Federal University of Rio Grande Do Sul, Av. Bento Gonçalves 9500, P.O. Box 15051, Porto Alegre, RS Postal Code 91501-970, Brazil
[2]Ion Beam Centre, Advanced Technology Institute, Faculty of Engineering and Physical Sciences, University of Surrey, Guildford, Surrey GU2 7XH, United Kingdom
Correspondence to: E. M. Stori (E-mail: elistori@gmail.com)

ABSTRACT: In this work, we explored the capabilities of energetic focused beams of light ions for the fabrication and analysis of microstructures produced on commercial polyethylene terephthalate (PET) foils. To that end, single lines and multi-structure patterns were drawn directly on the foils using Proton Beam Writing (PBW) techniques followed by chemical etching. The characterization of the microstructures was carried out with on-axis Scanning Transmission Ion Microscopy (STIM) employing H^{+1}, He^{+2}, and Li^{+3} ions in the MeV range. Scanning Electron Microscopy (SEM) was employed as well. The results show that a polymer like PET can be patterned trough a proper combination of irradiation parameters and etching times. However, aspect ratios obtained in this way are quite poor. Moreover, STIM images obtained from different regions of the ion energy spectra reveal patterns and cavities seen neither by conventional STIM, where the whole energy spectrum is used, nor by SEM. Moreover, striking differences are observed when different ions are used for STIM analysis. The results suggest that heavier ions provide additional information of the structures under analysis when compared with usual STIM employing protons. © 2015 Wiley Periodicals, Inc. J. Appl. Polym. Sci. **2016**, *133*, 43253.

INTRODUCTION

The modification of polymers induced by the passage of energetic ions is considered as an irreversible process since it causes permanent damage in the structure of the polymer. When MeV ions interact with matter, inelastic collisions lead to excitation and ionization of the atoms in the sample. Besides, in the case of polymers, the electronic excitation may cause a Coulomb explosion due to the non-conducting properties of the polymer, which leads to a localized excess of charge. In turn, all electrons generated due to the passage of energetic ions lose their energy through the interaction with atoms of the polymeric matrix, giving rise to free radicals, volatile components, new chemical bounds, scissions, and crosslinking events.[1,2]

Micromachining plays an important role in the fabrication of structures with a wide variety of technological applications.[3] Despite different techniques being applicable, the use of low energy ions in the keV range for micromachining purposes became a common choice with the advent of commercial Focused Ion Beam (FIB) systems, opening new possibilities in microsystem technology.[4] On the other hand, High Energy Focused Ion Beam (HEFIB)[5,6] employs MeV ions and has proved to be a powerful tool for applications requiring higher sputter yields. Proton Beam Writing (PBW) is a direct lithography technique, namely does not require any kind of masks, which can be used for patterning materials such as glasses, polymers or semiconductors.[7,8] The applications comprise different areas such as microfluidics, microphotonics, acoustic, filtering, biomaterials and tissue engineering, among others.[9–14] Moreover, structures made through PBW find straightforward application in the study of electroactive polymers.[15]

As far as polymers are concerned, polyimide, photoresist, PET (polyethylene terephthalate), and SU-8 among others have been used for the production of microelectromechanical systems due to their particular features including robustness, flexibility, biocompatibility, and even biodegradability.[16,17] However, microstructures obtained through energetic ion beams have been restricted to resist materials like PMMA (poly(methyl methacrylate)) and the epoxy-based SU-8. Indeed, these materials proved to be ideal for the production of three-dimensional structures with high aspect ratio through PBW.[18,19] Usually, silicon wafers

are spin-coated with thin layers of resist materials and the resulting samples are then cured through a thermal procedure.[20]

Scanning Transmission Ion Microscopy (STIM) is an ion microprobe technique that provides image formation obtained from the energy loss contrast of a focused ion beam transmitted through a thin sample. This technique is based on the energy loss of ions per unit length traversed in the medium, which is referred to as stopping power. The stopping power depends on the ion species, the material the ion is interacting with, and the energy of the ion. In general, the higher the ion mass the higher the stopping power. For instance, 1 MeV H^{+1}, 3 MeV He^{+2}, and 5.5 MeV Li^{+3} ions lose approximately 32, 164, and 344 electon-volts (eV) per nanometer traversed in mylar, respectively.[21]

STIM is considerably useful for the analysis of organic tissues and cells since they are composed mostly by light elements, thus enabling a sample thickness of tens of micrometers to be probed.[22–24] Different strategies based on the particle energy-loss spectrum can be employed for image processing purposes. Among the most common approaches are the mean and median image formation techniques, which require a statistical treatment of the energy loss spectrum. Another technique is based on the selection and analysis of particular regions of the energy loss spectrum.[25] Despite providing excellent results for simple cases, these techniques can lead to misinterpretation if the energy loss spectrum is complex.[22]

In principle, any ion can be used for STIM measurements. Due to practical reasons, protons are the most common choice for STIM experiments. However, hydrogen molecules[23] and alpha particles[24,26] have been used as well in cell analysis in the nanometer range. It is important to note that heavier ions provide better density contrast due to their higher stopping power. Conversely, heavier ions may jeopardize the energy resolution since the energy straggling is relatively higher than the proton case.[23,24]

The aim of the present work is twofold: (i) to use PBW followed by chemical etching to produce microstructures machined directly on free standing commercial PET foils; (ii) to explore the capabilities of STIM to analyze microstructures patterned on PET foils. To that end, parameters related to PBW and chemical etching were optimized. Moreover, STIM measurements were carried out with different ions, namely H^{+1}, He^{+2}, and Li^{+3}, while the respective energy loss spectra were divided into distinct energy regions. In this way, we were able to compare the performance of STIM analysis with different parameters.

MATERIALS AND METHODS

Different structures were fabricated through the PBW technique, namely a grid with 10×10 wells, a simple and double linear wells, and a step-like structure. Commercial polyethylene terephthalate (PET - Mylar®) foils of 1 cm^2 and 12 μm thick were irradiated at room temperature with 2.2 and 3 MeV protons. The beam spot size was about 2×2.5 μm^2 unless otherwise stated. An Oxford Microbeams® system operating in triplet mode coupled to a scanning system was used in all PBW and STIM experiments. The scanning system and all patterns were set to a 256×256 matrix (pixels). The pixel to micron ratio

was 1:1. Taking into account the beam spot size, an overlapping of the beam takes place at all pixels, thus ensuring that no gaps are generated in the patterned structures. Currents varied from 100 to 200 pA.

In order to study the role of the etching time and the fluence in the patterning of the PET foils, double linear patterns were drawn with a fixed fluence of 6×10^{15} ions cm^{-2} and with etching times from 5 to 60 min. In this case, 3 MeV protons were employed. Moreover, a grid consisting of 10×10 wells with dimension of 3×3 pixels and a fixed fluence of 6×10^{14} ions cm^{-2} was constructed with etching times varying from 30 s to 3 min. In this case, 2.2 MeV protons were employed. Finally, linear wells with fluences between 6×10^{13} and 6×10^{15} ions cm^{-2} and different etching times were built as well using 2.2 MeV protons.

A particular set of wells were obtained for analysis with STIM. In this case, the irradiation pattern was a line of 100×1 pixels with a fixed fluence of 6×10^{14} ions cm^{-2} and protons at 2.2 MeV. At this fluence, etching times as low as 1 min were enough to promote the total removal of the irradiated material. A total of four structures were fabricated for each etching time. The irradiation was controlled by the charge pulses per pixel in order to obtain the desired fluences.

In order to build the step-like structures, different fluences of 2.2 MeV protons were employed. In this way, a single etching procedure with fixed etching time could be used to produce structures with different thicknesses.[27] These structures consisted of an inner square irradiated with higher fluence (to guarantee the total removal of material from this region) and a larger outer square irradiated with lower fluence. The fluence of the inner square was fixed at 6×10^{14} ions cm^{-2}, while the fluences of the outer square were 6×10^{13}, 4×10^{13}, 3×10^{13}, and 1×10^{13} ions cm^{-2}. A pattern size of 30×30 pixels for the inner square and 75×75 pixels for the outer square was used in order to obtain the step-like structure.

After irradiation, the samples were submitted to an etching solution of $6M$ NaOH in a thermal bath at $(60 \pm 1)°C$ with continuous magnetic agitation. The time of the etching procedure varied from 1 to 20 min for the linear structures and was fixed at 3 min for the step-like structures.

The samples were analyzed by on-axis STIM using 1 MeV protons, 3 MeV alpha particles (He^{+2}), and 5.5 MeV Li^{+3} ions. For these measurements, the current was decreased to a few thousands ions s^{-1}. The analysis of the STIM spectra was based on the selection of distinct energy regions of the particle spectra. Each spectra was obtained in about 10 min. The respective images obtained through this procedure were used for qualitative and quantitative analysis. SEM measurements were performed as well for comparison purposes.

The dimensions of the structures were evaluated by a simple technique where lines intercepting the structures in convenient directions are drawn and the respective profiles are obtained. Dimensions are extracted from these profiles according to a procedure described elsewhere.[28] Finally, polymers with known thicknesses were measured and a calibration relating the peak position to the polymer thickness was obtained.
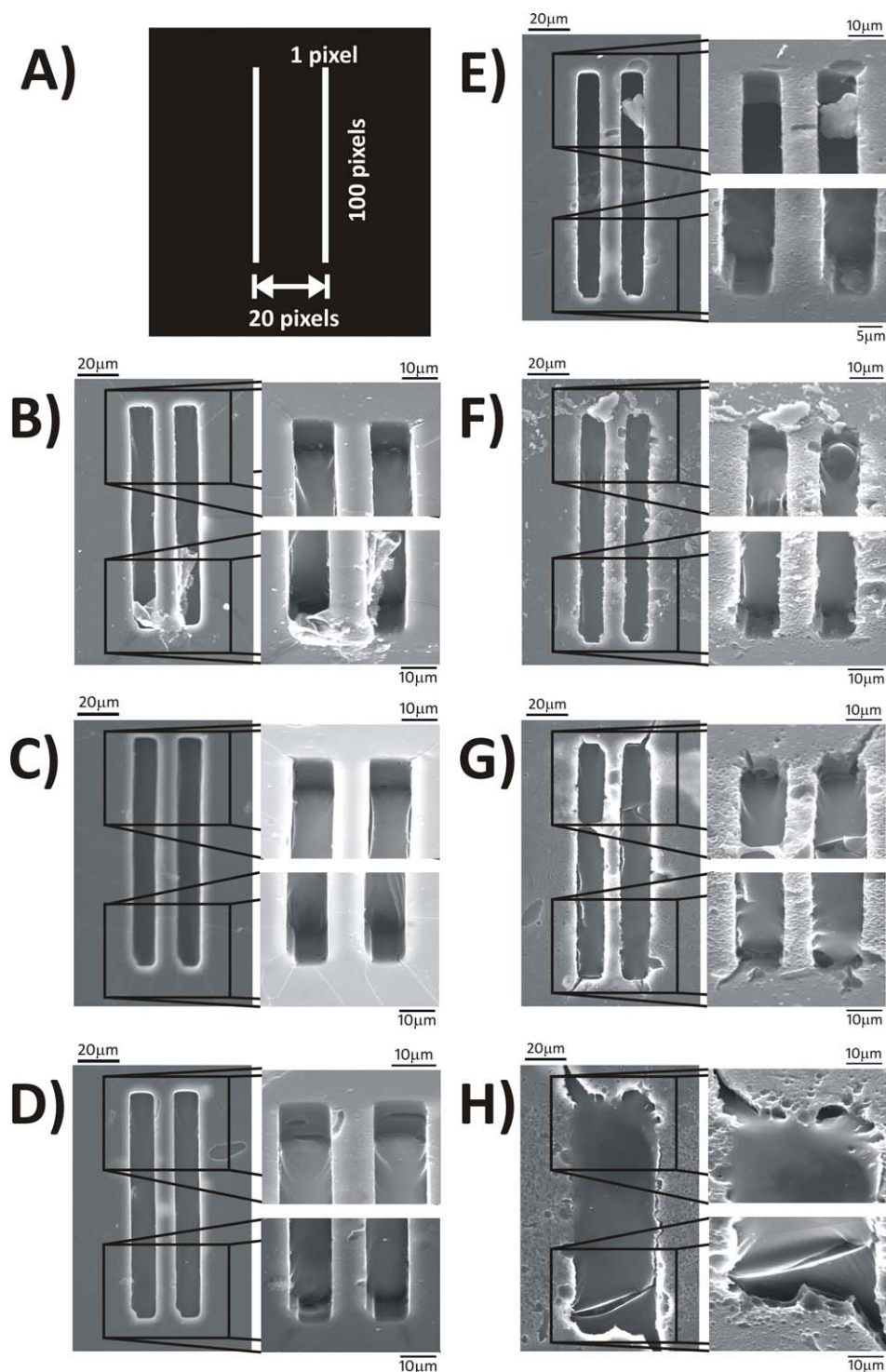
Figure 1. SEM images of parallel linear wells obtained with 3 MeV protons and a fixed fluence of 6×10^{15} ions cm^{-2}. Panel A shows the dimensions of the structures in terms of pixels. Panels B–H refers to etching times of 5, 10, 15, 20, 30 40, and 60 min, respectively. The insets show details of the marked regions. [Color figure can be viewed in the online issue, which is available at wileyonlinelibrary.com.]

RESULTS AND DISCUSSION

Figure 1 depicts SEM images of two linear wells obtained with an ion fluence of 6×10^{15} H^{+1} cm^{-2} and different etching times. For such a high fluence, relatively short etching times up to 20 min can lead to well-formed structures. Above 20 min of etching time, signs of degradation start to show up in the structures and become more severe as longer etching times are employed. These results show that the quality of the structure is strongly dependent on the etching time. In principle, high fluences require shorter etching times since the degree of damage
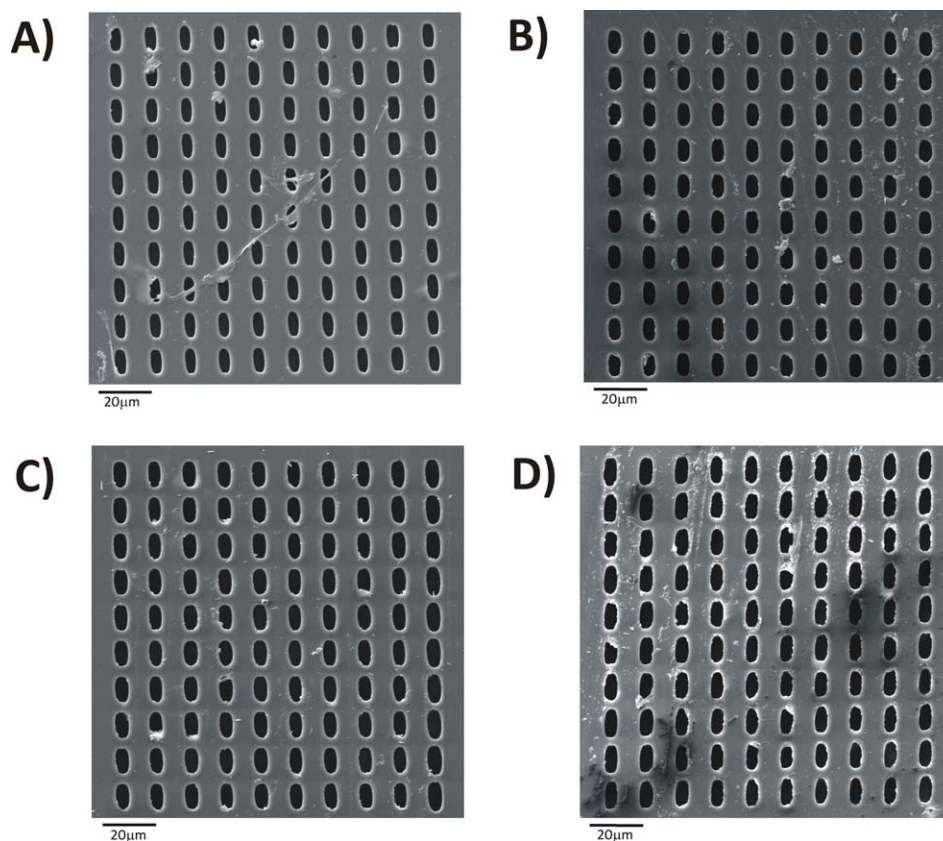
Figure 2. SEM images of a PET irradiated with 2.2 MeV protons with a fluence of 6×10^{14} ions cm^{-2}. The etching times were (A) 0.5, (B) 1, (C) 2 and (D) 3 min. [Color figure can be viewed in the online issue, which is available at wileyonlinelibrary.com.]

in the polymer depends on the number of ions interacting with it. Even fluences 10 times smaller can be developed by relatively short etching times as shown in Figure 2. In the present study, the corrosion of PET takes place mainly at ester groups (−COOR) which are hydrolyzed by the etching solution (NaOH), leading eventually to the production of −COO$^-$− and R−OH groups.[29] This mechanism is more efficient where the energy deposition due to the irradiation is high. Conversely, for periph-

eral regions close to the irradiated area the etching velocity is smaller, which requires longer exposure times to be developed. This is clearly seen in panels F, G, and H of Figure 1.

Figure 3 shows the etching times required to fully develop the linear well structures produced with different fluences. Very low fluences need relatively longer etching times to be developed. In this case, peripheral regions to the irradiated area are attacked as well, leading to irregular surfaces. For fluences up to
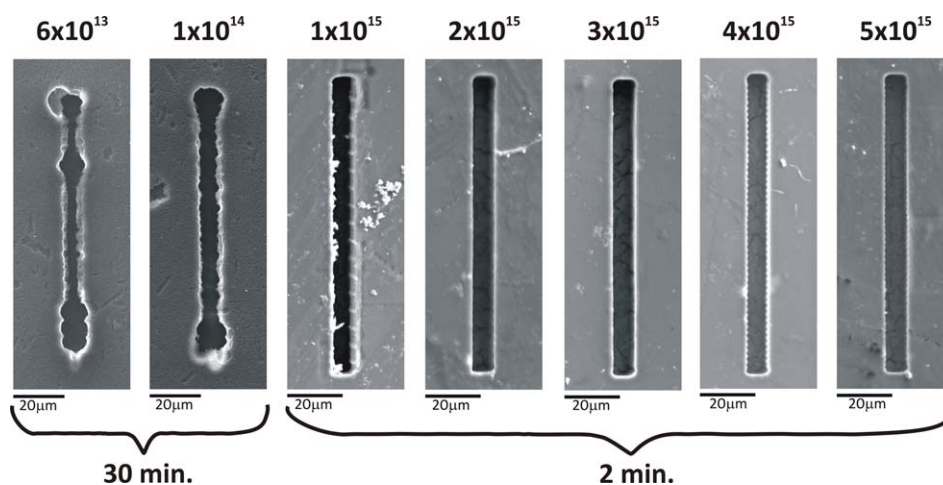

Figure 3. SEM images of linear wells obtained with different fluences (in units of ions cm^{-2}) and etching times (2 and 60 min). [Color figure can be viewed in the online issue, which is available at wileyonlinelibrary.com.]
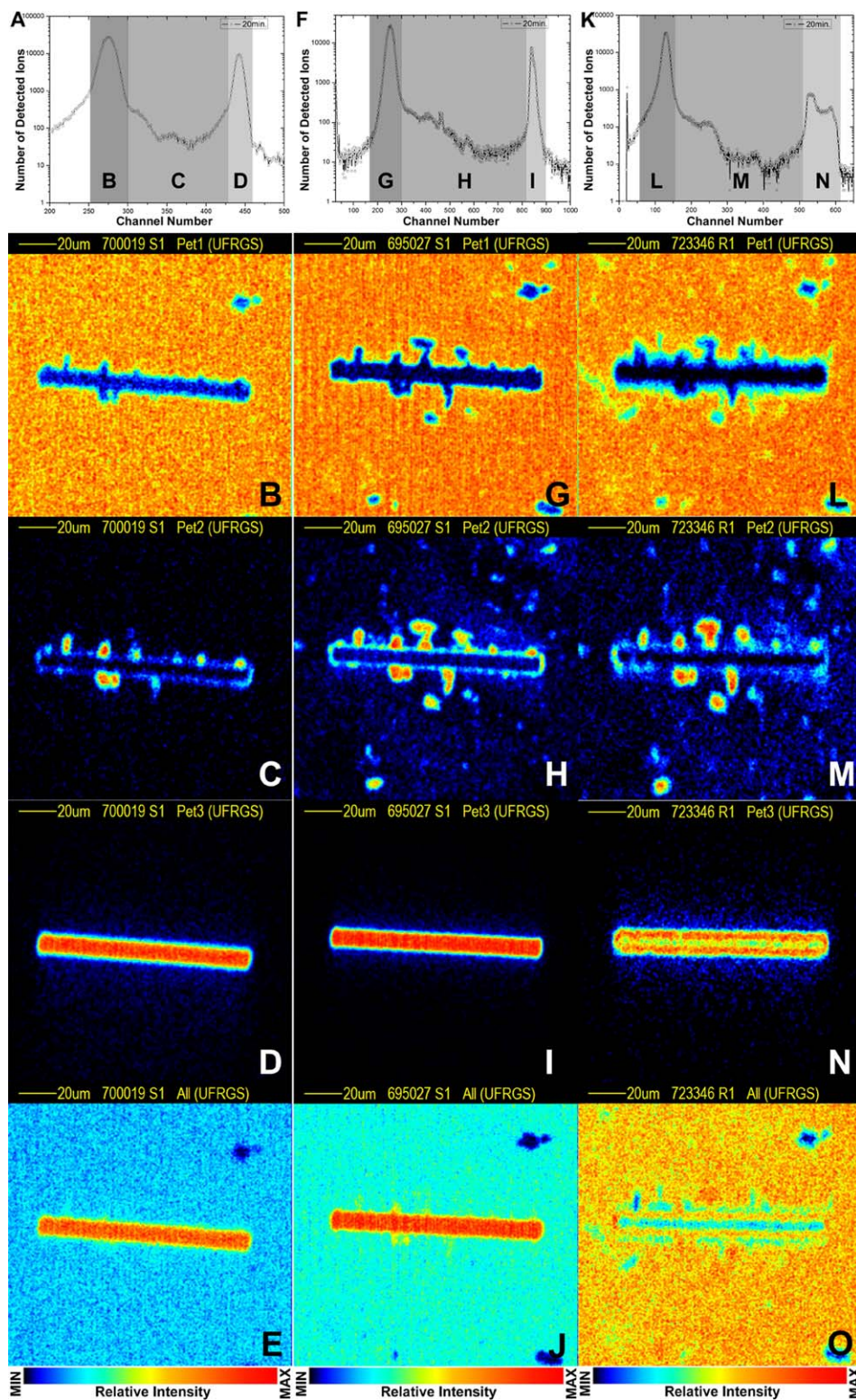
Figure 4. Energy loss spectra (number of detected ions per energy bin – channel number) and the respective on-axis STIM maps generated by H^{+1} (panels A, B, C, D, and E), He^{+2} (panels F, G, H, I, and J), and Li^{+3} (panels K, L, M, N, and O). The linear well was fabricated through PBW with subsequent chemical etching during 20 min. The letters on each energy loss spectra (panels A, F, and K) delineate the energy regions whose events were integrated in order to generate the respective STIM maps (panels B–D for protons, G–I for helium ions, and L–N for lithium ions). The bottom panels (E, J, and O) refer to the events integrated over the entire energy loss spectra. The channel number is linearly proportional to the particle energy and therefore increases with increasing energy of the transmitted ions. [Color figure can be viewed in the online issue, which is available at wileyonlinelibrary.com.]
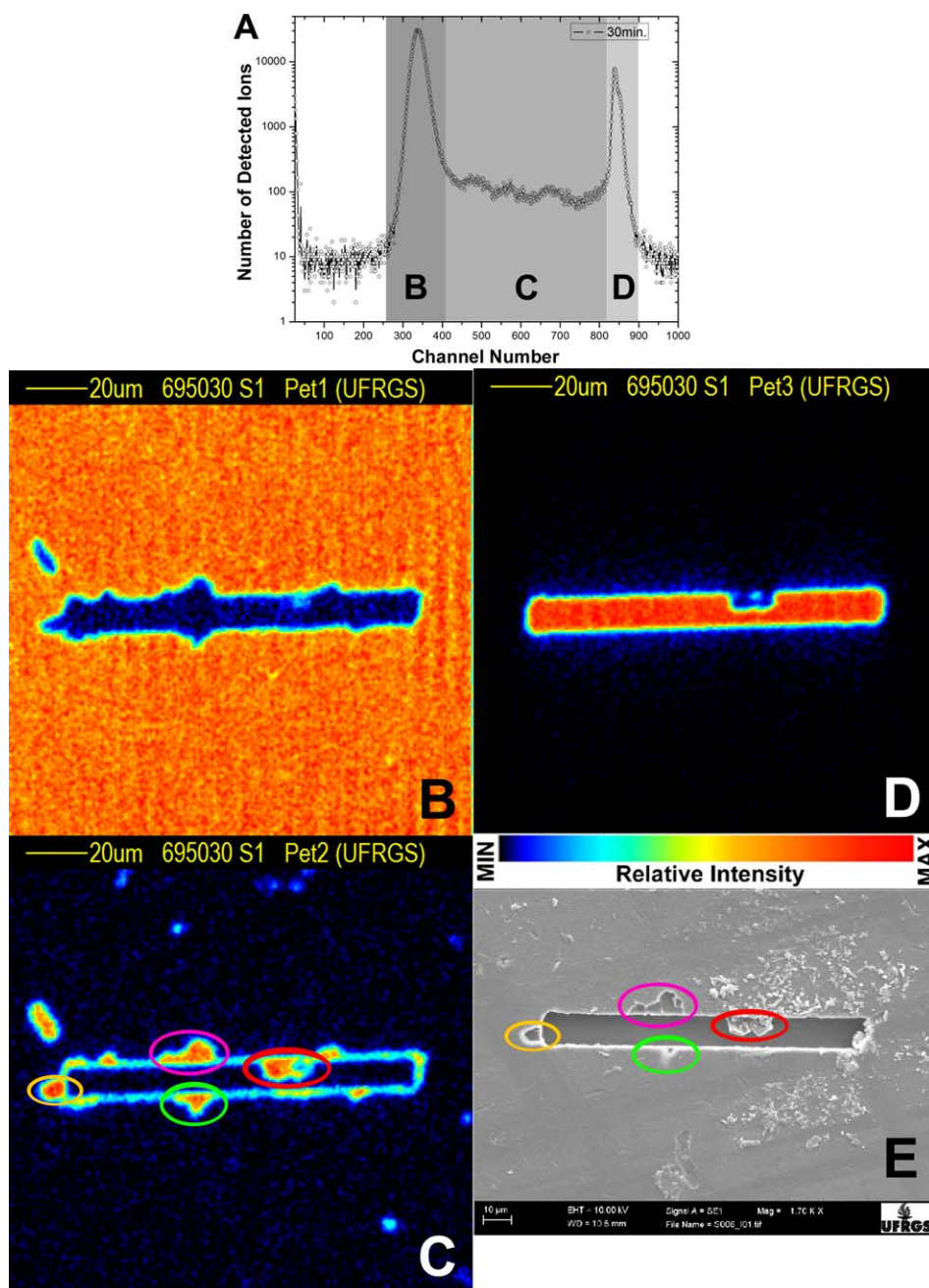
Figure 5. Energy loss spectra (number of detected ions per energy bin – channel number) and the respective on-axis STIM maps generated by He^{+2} (panels B, C, and D). Panel E depicts the respective SEM image. The linear well was fabricated through PBW with subsequent chemical etching during 30 min. For the sake of clarity, some substructures are marked with matching colors on panels C and E. The letters on the energy loss spectra (panel A) delineate the energy regions whose events were integrated in order to generate the respective STIM maps (panels B, C, and D). The channel number is linearly proportional to the particle energy and therefore increases with increasing energy of the transmitted ions. [Color figure can be viewed in the online issue, which is available at wileyonlinelibrary.com.]

5×10^{15} H^{+1} cm^{-2} we observe that very short etching times can be used to develop the structures. At these fluences, it has been observed that CO–O groups are the most affected by the irradiation with MeV ions heavier than protons.[30] Studies employing 0.48 MeV protons with fluences in the range $10^{13} - 10^{15}$ H^{+1} cm^{-2} have demonstrated that the oxygen density decreases as the fluence increases, indicating that oxygen is the most affected species during irradiation.[31]

The STIM measurements of the linear well performed with H^{+1}, He^{+2}, and Li^{+3} ions presented energy loss spectra containing three well distinct energy regions as shown in Figure 4 (panels A, F, and K). The high energy peaks located at the right end of the spectra refer to the perforated region of the sample, and thus are formed by the detection of ions that did not lose their initial energy. The peaks located at the low energy region of the spectra are formed by the detection of ions that passed
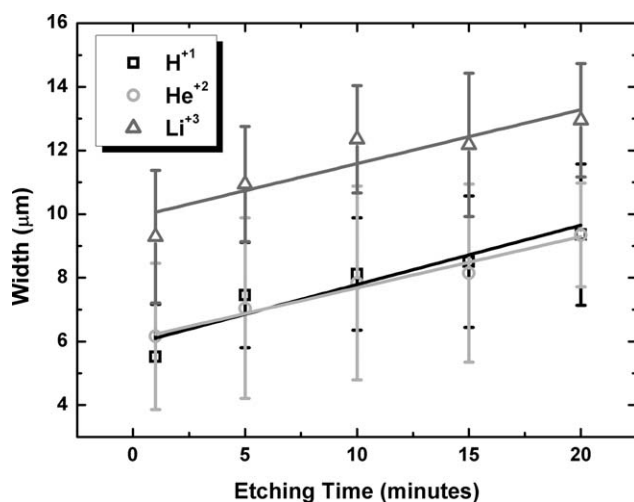
Figure 6. Width of the linear well as a function of the etching time obtained from the on-axis STIM maps with H^{+1} (squares), He^{+2} (circles), and Li^{+3} (triangles). The light gray, black, and dark gray lines stand for the least-square fittings to the H^{+1}, He^{+2}, and Li^{+3} data, respectively. Each data point and the corresponding uncertainty refer to the mean and standard deviation values of 16 measurements.

through the non-irradiated portions of the polymer, thus losing part of their initial energy. The region between the two peaks show some structures caused by irregularities with intermediate thicknesses. Once these regions are selected separately to generate STIM maps, different images are formed as shown in the panels of Figure 4. The lower panels of this figure (E, J, and O) depict the results obtained when no energy window is selected, i.e. the entire energy spectra are taken into account in order to generate STIM maps.

Figure 4 reveals that images obtained with He^{+2} (panels G, H, I, and J) and Li^{+3} (panels L, M, N, and O) ions provide information about buried structures or cavities barely observed with H^{+1} ions. This effect is caused by the relatively higher stopping power of heavier ions, thus making them more susceptible to smaller changes in density and thickness.[23] The cavities and porosity visible in the panels stem from the chemical attack of the PET foils after irradiation. Indeed, according to a previous work[28] where pristine etched and non-etched PET foils were analyzed by STIM and SEM, the porosity increases drastically with increasing etching times. Therefore, the etching procedure is the primary cause of the porosity. Moreover, the etching of non-irradiated areas is more important for longer etching times, causing the reduction of the thickness of the foils.

No substantial differences were observed between the results obtained with He^{+2} and Li^{+3} concerning the thickness/density resolution (panels G, H, I and L, M and N, respectively). However, it is visible that the structures obtained with Li^{+3} ions seem to be blurred while the images obtained with He^{+2} ions are sharper. This effect was attributed to the way the ion current was reduced in both cases for the STIM measurements. For protons and alpha particles, the objective slits were reduced and the beam was defocused in order to achieve count rates of the order of a few thousands of ions per second. For the Li^{+3}

beam, the initial current was considerably low and any reduction of the objective slits would decrease the current to unacceptable levels. Therefore, the desirable count rate was achieved by just defocusing the beam, thus keeping a relatively larger aperture for the objective slits. For that reason, the lateral resolution was compromised when Li^{+3} ions were used. The beam size, in this case, was approximately $3 \times 3.5 \ \mu m^2$.

Another anomalous effect was observed when using Li^{+3} beam, as shown in panel N of Figure 4, which depicts the STIM map related to the high energy peak of the linear well. It can be observed that the map shows higher concentration of ions on the borders of the structure. Actually, the energy loss spectrum (panel K) displays a broad high-energy structure consisting of two peaks, which leads to the differences shown in the STIM map. Although we have no explanation for that, this effect could be related to charge effects in the borders of the structures, defocusing the transmitted ions through the hole.

Figure 5 shows a comparison between STIM and SEM images of the same structure. A few carved substructures can be seen in both images. However, there are some structures not visible on the SEM image. Basically, SEM provides information of the surface of the sample due to the relatively shallow penetration of electrons in the polymer. In this case, SEM is not sensitive to deep buried structures. Besides, conventional SEM requires coating of insulating samples, which may change the surface of the sample or even hide some structures. Conversely, STIM is not destructive and more reliable once it does not demand any treatment of the sample and employs energetic ions that go through the sample. Moreover, all information concerning the dimensions of the structures can be extracted from a single STIM measurement, while SEM may require extra images for thickness measurements. Finally, since STIM is not destructive, the samples can be used for other purposes once the STIM
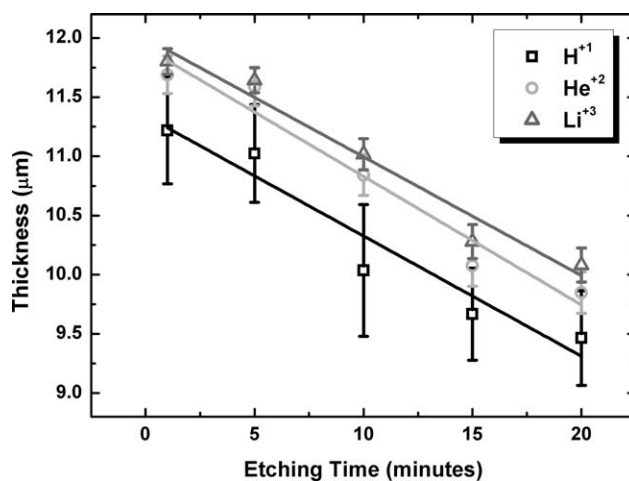

Figure 7. Thickness of the non-irradiated portions of the polymer as a function of the etching time obtained from the on-axis STIM maps with H^{+1} (squares), He^{+2} (circles), and Li^{+3} (triangles). The light gray, black, and dark gray lines stand for the least-square fittings to the H^{+1}, He^{+2}, and Li^{+3} data, respectively. Each data point and the corresponding uncertainty refer to the mean and standard deviation values of four measurements. See text for further information.
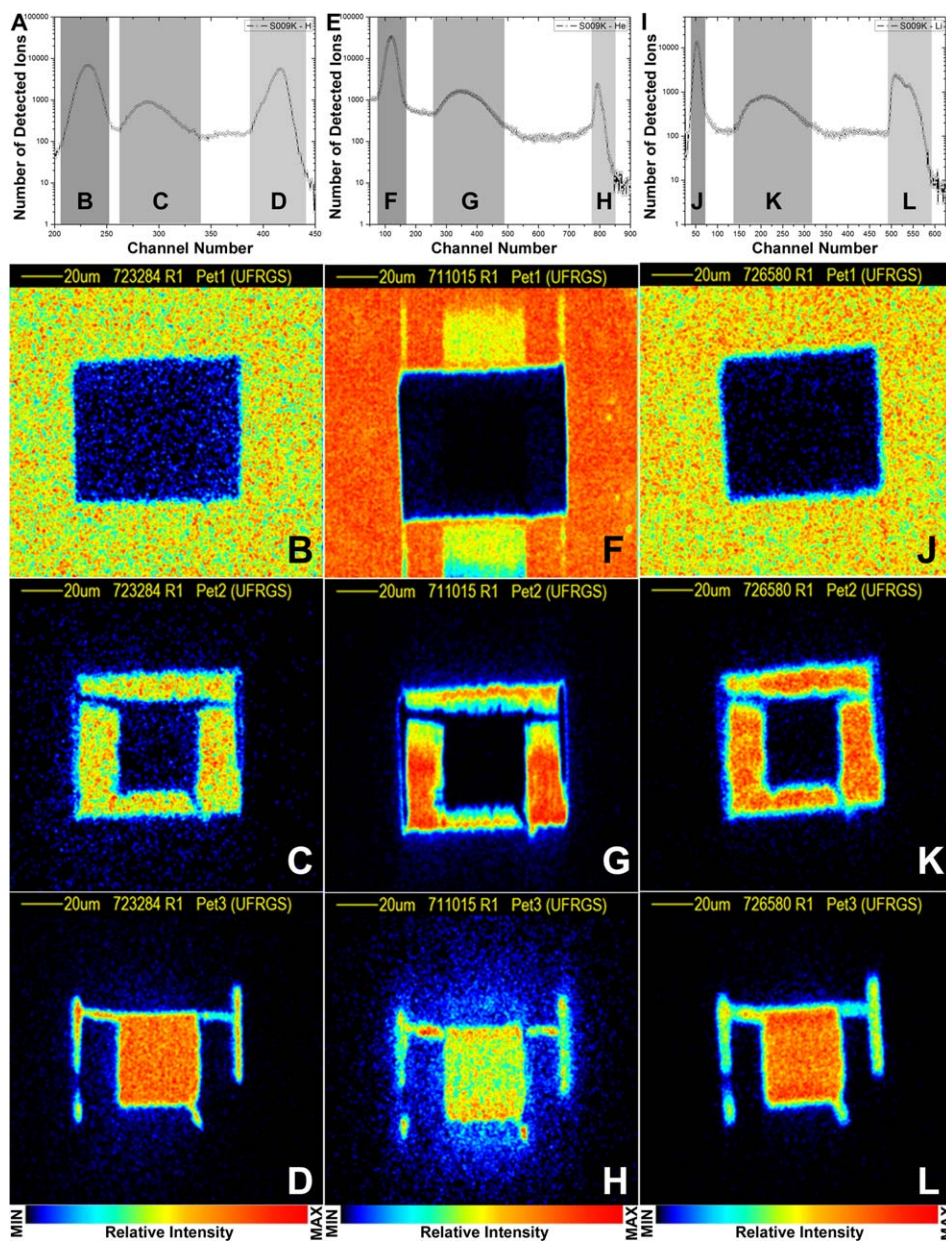
Figure 8. Energy loss spectra (number of detected ions per energy bin – channel number) and respective on-axis STIM maps generated by H^{+1} (panels A, B, C, and D), He^{+2} (panels E, F, G, and H) and Li^{+3} (panels I, J, K, and L). The step-like structure was fabricated through PBW with fluences of 6×10^{14} and 3×10^{13} ions cm^{-2} for the inner and outer squares, respectively. The sizes of the inner and outer squares were approximately 30×30 μm^2 and 75×75 μm^2, respectively. The etching time was 3 min. The letters on each energy loss spectra (panels A, E, and I) delineate the energy regions whose events were integrated in order to generate the respective STIM maps (panels B, C, and D for protons; F, G, and H for helium ions; and J, K, and L for lithium ions). The channel number is linearly proportional to the particle energy and therefore increases with increasing energy of the transmitted ions. [Color figure can be viewed in the online issue, which is available at wileyonlinelibrary.com.]

measurements are done. This is not the case for SEM since the coating and mounting of the samples may turn them not viable for subsequent analyses.

The width of the linear well and the thickness of the polymer were evaluated from the STIM maps.[28] The results obtained using different ions are shown in Figures 6 and 7, respectively. Concerning the width, each of the four samples was measured four times, thus totaling 16 measurements for each data point shown in Figure 6. This figure reveals that the same etching

ratio (about 0.17 μm min^{-1}) is obtained regardless the ion used in the analysis. The positive slope indicates that the width of the structures increases as the etching time increases. Indeed, once all irradiated material is removed by the solution, more non-irradiated portions of the polymer are carved by the etching procedure.[28]

The dimensions of the final structures are relatively larger than those expected from the patterning procedure. This effect is related to the nature of the ion-matter interaction. In order to
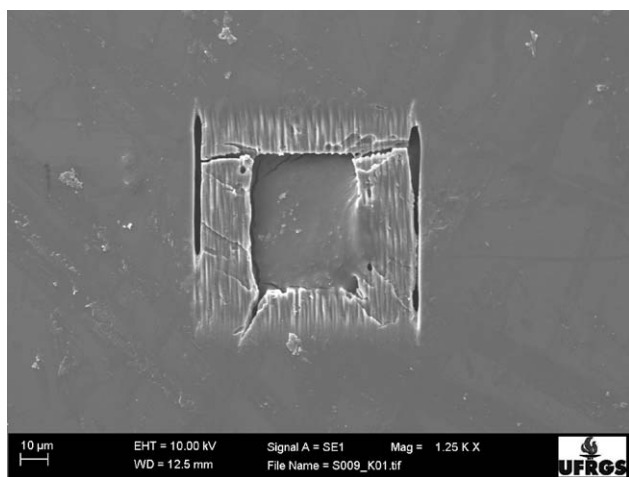
Figure 9. SEM image depicting the step-like structure shown in Figure 5.

check that, a simulation of ion trajectories was carried out using the TRIM (Transport of Ions in Matter) package.[21] According to the simulation, 2.2 MeV protons lose about 20 keV per μm traversed in PET foils. More importantly, the lateral straggling (i.e. the deviation of the particles with respect to their primary straight trajectory inside the polymer after traversing a certain depth) is about 2.2 μm. If it is taken into account that, during irradiation, the beam size is about twice the pixel size, we would have, as a final result, a structure enlarged by around 2.7 μm in each direction. Finally, other effects like ion fluence may have an impact on the energy density deposited in the foil and, consequently, on the lateral range of damage caused by the energetic ion. All these effects lead to an enlargement of the structures as shown in this work.

The thicknesses of the samples were also studied with different ions and the results are shown in Figure 7. In this case, only four measurements were carried out for each etching time, as this information is obtained directly from the energy loss spectra. Once more, the etching ratio provided by all ions is compatible with each other (about $- 0.10$ μm min^{-1}). The data present a negative slope because the longer the etching time the thinner the non-irradiated polymer becomes. Moreover, the proton data is shifted downwards by about 0.5 μm with respect to the results provided by He^{+2} and Li^{+3}. However, it must be pointed out that from the statistical point of view, the majority of the data are compatible to each other, i.e. they are statistically the same. Finally, it is important to note that the results provided by He^{+2} and Li^{+3} are presumably more reliable than those provided by protons due to their best density contrast.

For the step-like structures, it was observed that fluences of 6×10^{13} and 4×10^{13} ions cm^{-2} were not effective for the production of such structures since all the irradiated area of the hollow outer square was removed by the etching solution in 3 min. For the fluence of 1×10^{13} ions cm^{-2}, the step was formed, but it was too thick to resolve the irradiated from the non-irradiated part of the polymer. Therefore, the ideal fluence for a fixed etching time of 3 min was found to be 3×10^{13} ions cm^{-2}. The results are shown in Figure 8 for protons

(panels A, B, C, and D), helium (panels E, F, G, and H), and lithium (panels I, J, K, and L). Panels A, E, and I reveal three distinct peaks. The intermediate peaks refer to the step as shown in panels C, G, and K. These intermediate peaks are relatively broader than the others. This effect is due to irregularities in the formation of the step. Indeed, Figure 9 shows the SEM image of the structure and reveals that the step surface is not smooth as the non-irradiated portions of the polymer. This effect is related to the superposition of the beam[27,28] since the beam spot size is about twice the size of the pixel. A careful inspection of panel G of Figure 5 reveals the same structures as observed by SEM. Finally, the values for the thickness of the step measured with H^{+1}, He^{+2}, and Li^{+3} were (8.6 ± 0.8) μm, (8.5 ± 0.8) μm, and (8.2 ± 0.9) μm, respectively.

CONCLUDING REMARKS

In this work, a study of PET foils structured directly by PBW and analyzed with on-axis STIM using three different ion beams (H^{+1}, He^{+2}, and Li^{+3}) was carried out. To that end, different types of structures were produced, namely a grid with 10×10 wells, a double linear well, a linear well and a step-like structure.

Concerning the patterning of PET foils, the present results shows that a proper combination of irradiation parameters and post-irradiation chemical etching can be used to produce simple and complex structures in a polymer in a straightforward manner. It has been demonstrated that very low fluences require longer etching times, which eventually leads to the degradation of non-irradiated portions of the polymer. Higher fluences demand shorter etching times. Therefore, a proper balance between the fluence employed during the irradiation and the etching time used to develop the structure may lead to better results in terms of aspect ratio. Furthermore, the lateral straggling plays an important role at the enlargement of the final structures beyond the beam size. In general, it must be noted that the structures on PET foils obtained through ion irradiation and subsequent etching have relatively poor aspect ratios, which may limit the use of this technique to some applications where high aspect ratios are not needed. For instance, such structures (with and without post-irradiation etching) can be used for the confinement and oriented growth of cells since they can attach to the damaged portions of the polymer caused by the impact of energetic ions.

It is important to draw attention to the fact that a mismatch between the pixel size and the beam spot size may lead to ridges and roughness of the surface when the irradiated area is not fully corroded by the chemical attack. This problem may be overcome with the reduction of the beam spot-size or a change in the pixel to micrometer ratio. In this way, overlaps of the beam can be brought to a minimum, thus improving the aspect ratio of the final structure.

The use of energy windows selected from the STIM energy loss spectra proved to be a powerful tool for the analysis of microstructures produced by PBW followed by chemical etching. Moreover, the use of heavier ions reveals cavities and buried structures not seen neither with STIM measurements carried out with protons nor with SEM. In this respect, Li^{+3} ions are

better than alpha particles at the expense of the lateral resolution. Therefore, for this particular study, the ion that provides the best density contrast without compromising the spatial resolution is He^{+2}.

REFERENCES

1. MacKová, A.; Havránek, V.; Švorčík, V.; Djourelov, N.; Suzuki, T. *Nucl. Instrum. Methods Phys. Res. B* **2005**, *240*, 245.

2. Djebara, M.; Stoquert, J. P.; Abdesselam, M.; Muller, D.; Chami, A. C. *Nucl. Instrum Methods Phys. Res. B* **2012**, *274*, 70.

3. Madou, M. J. Fundamentals of Microfabrication; CRC Press: Boca Raton, **1997**.

4. Reyntjens, S.; Puers, R. *J. Micromech. Microeng.* **2001**, *11*, 287.

5. Glass, G. A.; Dias, J. F.; Dymnikov, A. D.; Rout, B. *Nucl. Instrum. Methods Phys. Res. B* **2008**, *266*, 3330.

6. Glass, G. A.; Dias, J. F.; Dymnikov, A. D.; Houston, L. M.; Rout, B. *J. Micro/Nanolithog. MEMS MOEMS* **2009**, *8*, 013013.

7. Mistry, P.; Gomez-Morilla, I.; Grime, G. W.; Webb, R. P.; Gwilliam, R.; Cansell, A.; Merchant, M.; Kirkby, K. J.; Teo, E. J.; Breese, M. B. H.; Bettiol, A.; Blackwood, D. J.; Watt, F. *Nucl. Instrum. Methods Phys. Res. B* **2005**, *237*, 188.

8. Bettiol, A. A.; Sum, T. C.; Cheong, F. C.; Sow, C. H.; Venugopal Rao, S.; van Kan, J.; Teo, E. J.; Ansari, K.; Watt, F. *Nucl. Instrum. Methods Phys. Res. B* **2005**, *231*, 364.

9. Udalagama, C.; Teo, E. J.; Chan, S. F.; Kumar, V. S.; Bettiol, A.; Watt, F. *Nucl. Instrum. Methods Phys. Res. B* **2011**, *269*, 2417.

10. Larisch, W.; Koal, T.; Werner, R.; Hohlweg, M.; Reinert, T.; Butz, T. *Nucl. Instrum. Methods Phys. Res. B* **2011**, *269*, 2444.

11. Scholz, U.; Menzel, F.; Pluta, M.; Grill, W.; Butz, T. *Nucl. Instrum. Methods Phys. Res. B* **2011**, *269*, 2452.

12. Menzel, F.; Spemann, D.; Lenzner, J.; Böhlmann, W.; Zimmermann, G.; Butz, T. *Nucl. Instrum. Methods Phys. Res. B* **2009**, *267*, 2321.

13. Ng, C. K. M.; Tjhin, V. T.; Lin, A. C. C.; Cheng, J. P.; Cheng, S. H.; Yu, K. N. *Nucl. Instrum. Methods Phys. Res. B* **2012**, *278*, 15.

14. Furuta, Y.; Nishikawa, H.; Satoh, T.; Ishii, Y.; Kamiya, T.; Nakao, R.; Uchida, S. *Nucl. Instrum. Methods Phys. Res. B* **2009**, *267*, 2285.

15. Souza, C. T.; Stori, E. M.; Fink, D.; Vacík, V.; Švorčík, V.; Papaléo, R. M.; Amaral, L.; Dias, J. F. *Nucl. Instrum. Methods Phys. Res. B* **2013**, *306*, 222.

16. Armani, D. K.; Liu, C. *J. Micromech. Microeng.* **2000**, *10*, 80.

17. Kim, E.; Xia, Y.; Whitesides, G. M. *Lett. Nat.* **1995**, *376*, 581.

18. Van Kan, J. A.; Shao, P. G.; Ansari, K.; Bettiol, A.; Osipowicz, T.; Watt, F. *Microsyst. Technol.* **2007**, *13*, 431.

19. Van Kan, J.; Bettiol, A.; Ansari, K.; Teo, E. J.; Sum, T. C.; Watt, F. *Int. J. Nanotechnol.* **2004**, *1*, 464.

20. Van Kan, J. A.; Sanchez, J. L.; Xu, B.; Osipowicz, T.; Watt, F. *Nucl. Instrum. Methods Phys. Res. B* **1999**, *158*, 179.

21. Ziegler, J. F.; Biersack, J. P.; Littmark, U. The Stopping and Range of Ions in Solids; Pergamon Press: New York, **1985**.

22. Bench, G.; Saint, A.; Legge, G. J. F.; Cholewa, M. *Nucl. Instrum. Methods Phys. Res. B* **1993**, *77*, 175.

23. Ren, M.; van Kan, J.; Bettiol, A.; Daina, L.; Gek, C. Y.; Huat, B. B.; Whitlow, H. J.; Osipowicz, T.; Watt, F. *Nucl. Instrum. Methods Phys. Res. B* **2007**, *260*, 124.

24. Watt, F.; Bettiol, A. A.; van Kan, J. A.; Ynsa, M. D.; Minqin, R.; Rajendran, R.; Huifang, C.; Fwu-Shen, S.; Jenner, A. M. *Nucl. Instrum. Methods Phys. Res. B* **2009**, *267*, 2113.

25. Rajta, I.; Gál, G. A. B.; Szilasi, S. Z.; Juhász, Z.; Biri, S.; Mátéfi-Tempfli, M.; Mátéfi-Tempfli, S. *Nanotechnology* **2010**, *21*, 295704.

26. Chen, X.; Chen, C. B.; Udalagama, C. N. B.; Ren, M.; Fong, K. E.; Yung, L. Y. L.; Giorgia, P.; Bettiol, A. A.; Watt, F. *Biophys. J.* **2013**, *104*, 1419.

27. Menzel, F.; Spemann, D.; Koal, T.; Butz, T. *Nucl. Instrum. Methods Phys. Res. B* **2011**, *269*, 2427.

28. Stori, E. M.; de Souza, C. T.; Amaral, L.; Fink, D.; Papaléo, R. M.; Dias, J. F. *Nucl. Instrum. Methods Phys. Res. B* **2013**, *306*, 99.

29. Spohr, R. *Eur. Res. Train. Netw. EuNITT* **2001**, *1*,

30. Bridwell, L. B.; Giedd, R. E.; Wang, Y. Q.; Mohite, S. S.; Jahnke, T.; Brown, I. M.; Bedell, C. J.; Sofield, C. J. *Nucl. Instrum. Methods Phys. Res. B* **1991**, *56/57*, 656.

31. Abdesselam, M.; Stoquert, J. P.; Chami, S.; Djebara, M.; Chami, A. C.; Siad, M. *Nucl. Instrum. Methods Phys. Res. B* **2009**, *267*, 108.